

Influence of dislocations in multilayer graphene stacks: A phase field crystal study

K. R. Elder,¹ Zhi-Feng Huang,² and T. Ala-Nissila^{3,4}

¹*Department of Physics, Oakland University, Rochester, Michigan 48309, USA*

²*Department of Physics and Astronomy, Wayne State University, Detroit, Michigan 48201, USA*

³*QTF Centre of Excellence, Department of Applied Physics,
Aalto University, P.O. Box 15600, FI-00076 Aalto, Espoo, Finland*

⁴*Interdisciplinary Centre for Mathematical Modelling, Department of Mathematical Sciences,
Loughborough University, Loughborough, Leicestershire LE11 3TU, UK*

In this work the influence of 5|7 dislocations in multilayer graphene stacks (up to six layers) is examined. The study is conducted through a recently developed Phase Field Crystal (PFC) model for multilayer systems incorporating out-of-plane deformations and parameterized to match to density functional theory calculations for graphene bilayers and other systems. The specific configuration considered consists of one monolayer containing four 5|7 dislocations (i.e., two dislocation dipoles) sandwiched in between perfect graphene layers. The study reveals how the strain field from the dislocations in the defected layer leads to out-of-plane deformations that in turn cause deformations of neighboring layers. Quantitative predictions are made for the defect free energy of the multilayer stacks as compared to a defect-free system, which is shown to increase with the number of layers and system size. Furthermore it is predicted that system defect energy saturates by roughly ten sheets in the stack, indicating the range of defect influence across the multilayer. Variations of stress field distribution and layer height profiles in different layer of the stack are also quantitatively identified.

I. INTRODUCTION

Since the discovery of graphene (Gr) [1], monolayers of various two-dimensional (2D) materials have been the focus of many research studies due to their potential use in technological applications. Currently a vast collection of materials can exhibit stable (free-standing or supported) 2D structures, such as Gr and its various allotropes, silicene (Si), phosphorene (P), hexagonal boron nitride (hBN), MoS₂, NbSe₂, and SnTe, among many others. Some of them display an extraordinary variety of correlated magnetic and electronic states [2, 3]. Their range of physical properties can be further varied by combining them either laterally or vertically. Selected immiscible materials such as Gr and hBN can even coexist within a single 2D layer [4], and in-plane heterostructures or lateral multijunctions of transition-metal dichalcogenides (TMDs) can be grown via edge epitaxy [5, 6]. Also importantly, due to the dominant dispersive van der Waals (vdW) forces between layers, it is possible to stack them into coupled 2D multilayers (s2D) that can be either identical such as in multilayer Gr or form heterogeneous vdW structures from different materials such as Gr and hBN or different types of TMDs.

Stacked layers of vdW materials can be further twisted or translated relative to each other. This often leads to exotic material patterns, phenomena, and properties. For example, twisted Gr bi- and multilayer s2D systems lead to complex “flamingo” type Moiré patterns [7] and generate novel correlated states of matter such as heavy fermions [8] and van Hove singularities [9]. One of the most spectacular examples is that twisted Gr bilayers exhibit superconductivity at a “magic” twist angle ($\approx 1^\circ$) [10, 11]. The number of possible stacking combinations of 1D/2D/3D materials is enormously large and will remain an active field of research for a long time to come.

The focus of our work here is on multiple layers of Gr with one layer containing 5|7 defects. In general such defected states and others (such as the superlattice Moiré patterns discussed above) can significantly alter electrical, thermal and mechanical properties in 2D materials and their stacking. Defects, including dislocations, grain boundaries, and impurities, often strongly influence material properties, such as thermal resistance in polycrystal Gr [12] and hBN [13]. Gong *et al.* [14] have shown that in a Gr bilayer, with one layer containing a point defect, the barrier for defect migration is increased by 9 – 14% compared to a single monolayer, while Choi *et al.* [15] found that the spin magnetic moment near a monovacancy in Gr is reduced when another Gr layer is added. Recent experiments by Mohapatra *et al.* [16] have shown that even wrinkles in few-layer Gr materials can increase the thermal conductivity (κ) from 165 W/mK in pristine regions to 225 W/mK near wrinkled regions. Thus it is important to understand the impact of defects in these quasi-2D systems.

In this paper the influence of 5|7 dislocation defects in one layer of Gr in (or close to) the middle of a stack of Gr multilayers is considered. Our study is based on a 2D phase field crystal model which allows for out-of-plane deformations [17]. In general PFC methods have an advantage over atomistic methods (e.g., molecular dynamics) in that the simulation timescale is controlled by diffusive time scales as opposed to vibrational scales. In addition, PFC models are based on system free energies, not atomic potentials, so that entropy, for example, is naturally incorporated. The out-of-plane PFC model has been applied to study 5|7 defects in a single Gr layer and predicted an energy of 6.8 eV which is similar to that from quantum-mechanical density functional theory (DFT) calculations of Chen and Chrzan [18] (6.17 eV) and Yazyev and Louie [19] (7.5 eV), and molecu-

lar dynamics calculations of Liu and Yakobson [20] (5.0 eV). The model has also been used to identify the scaling behavior of height fluctuations in both pinned and free-standing Gr monolayers [21, 22] as well as Moiré patterns in Gr/hBN bilayers [23]. The results of these prior studies were consistent with prior experiments, simulations and theoretical predictions. Furthermore the interaction between Gr layers was parameterized to match the stacking energies and heights predicted by DFT calculations of Zhou *et al.* [24] as discussed in Sec. II.

The paper is structured as follows. In Sec. II the methodology and model parameterization used are presented for the study of multiple layers of stacked Gr. In Sec. III the influence of two dislocation dipoles (each containing two 5|7 defects) within one layer surrounded by other pristine Gr layers is examined, with predictions of system energy, stress field distribution, and layer height profiles as well as their variations on the number of stacking layers and system size provided. Finally in Sec. IV a discussion and summary of the results are provided.

II. METHODOLOGY

Consider a stack of M layers each of which is described by a 2D dimensionless atomic number density variation field, $n_i(x, y)$, and a height, $h_i(x, y)$. As discussed in a prior publication [17] a free energy functional F_i that is minimized by a periodic array of maxima in n_i and allows for out-of-plane deformations can be written as

$$\frac{F_i}{c_g} = \int d\vec{r} \left[\frac{\Delta B}{2} n_i^2 + \frac{B^x}{2} (\mathcal{L}_w n_i)^2 + \frac{\tau}{3} n_i^3 + \frac{v}{4} n_i^4 + \frac{\kappa}{2} \int d\vec{r}' C(|\vec{r} - \vec{r}'|) h_i(\vec{r}) h_i(\vec{r}') \right], \quad (1)$$

where

$$\mathcal{L}_w = 1 + \nabla^2 - (h_x^2 \partial_x^2 + h_y^2 \partial_y^2 + 2h_x h_y \partial_x \partial_y), \quad (2)$$

with $h_x = \partial_x h_i$, $h_y = \partial_y h_i$, and $\nabla^2 = \partial_x^2 + \partial_y^2$. The last term in Eq. (1) accounts for the bending energy of the plane and the parameter κ is the bending energy coefficient. The Fourier transform of kernel C is set as $\hat{C}_k = -k^4$ for wave number $k < 1/2$ and $\hat{C}_k = -10^4$ for $k > 1/2$, to suppress short range fluctuations in the height. The results reported here were found to be insensitive to the choice of this \hat{C}_k cutoff, as long as the cutoff was large enough to eliminate short range fluctuations in h but short enough to not change the dislocation core configuration or energy. The parameters for graphene are set to $(c_g, \Delta B, B^x, \tau, v, \kappa, \bar{n}_i) = (6.58\text{eV}, -0.15, 0.874818, 1, 0.209726, 0)$, where \bar{n}_i is the average density value of n_i . For these parameters the lowest energy state is a 2D honeycomb array of density maxima and the energy of a 5|7 defect has been calculated to be 6.8 eV.

For a bilayer system the direct coupling between layers occurs through

$$F_{ij}^c = \int d\vec{r} \left[\sum_{l=1}^2 V_0^{(l)} (\delta n_i \delta n_j)^l + a_2 (\Delta h_{ij} - \Delta h_{ij}^0)^2 \right], \quad (3)$$

where $\Delta h_{ij} = h_i - h_j$, $\delta n_i = n_i - \bar{n}_i$ and $\Delta h_{ij}^0 = \Delta(1 + \alpha \delta n_i \delta n_j)$. As discussed in Ref. [17], the coupling parameters $V_0^{(1)}, V_0^{(2)}, \alpha_2, \Delta$, and α can be fit to the stacking energies and heights that were calculated by Zhou *et al.* [24] using quantum-mechanical density functional theory (DFT) (more specifically the computationally expensive, but more accurate, ACFDT-RPA results as used in this work). For a system of M layers this can easily be extended by assuming each layer only interacts with neighbouring layers (via Eq. (3)). The goal of this work is to determine the lowest energy states for a set of layers with one of them containing defects. The free energy minimization is obtained by relaxational dynamics, i.e.,

$$\frac{\partial n_i}{\partial t} = -\frac{\delta F_t}{\delta n_i}; \quad (4)$$

$$\frac{\partial h_i}{\partial t} = -\Gamma \frac{\delta F_t}{\delta h_i}, \quad (5)$$

where $i = 1, 2, \dots, M$, Γ is the mobility for layer height, and F_t is the sum of the free energies of all layers and their interaction energy (F^c), i.e.,

$$F_t = \sum_{i=1}^M F_i + \sum_{i=1}^{M-1} F_{i+1,i}^c = \sum_{i=1}^M F_i + F^c. \quad (6)$$

Simulations were performed on the xy plane with periodic boundary conditions, using the semi-implicit method in Fourier space as described in Ref. [25] Appendix B 4. The average value of n_i for each layer was fixed (i.e., the $k = 0$ Fourier mode of n_i was never changed). For the largest system size studied here (i.e., six layers with each of size 138 nm \times 69 nm), relaxation to a steady state could take considerable amount of computational time, on the order of one month in a single GPU.

In general a one-mode approximation for the density field, i.e.,

$$n_i = \bar{n}_i + 2\phi \sum_{j=1}^3 \cos(\vec{G}_j \cdot \vec{r}), \quad (7)$$

was typically used as the initial state, where the reciprocal lattice vectors are $\vec{G}_1 = (-\sqrt{3}q_x/2, -q_y/2)$, $\vec{G}_2 = (0, q_y)$, and $\vec{G}_3 = (\sqrt{3}q_x/2, -q_y/2)$. In this approximation the values of ϕ , q_x and q_y that minimize the free energy are given by

$$\phi_{\text{eq}} = \frac{3\bar{n}_i v + \tau + \sqrt{\tau^2 - 15v\Delta B - 4\bar{n}_i v(6\tau + 9\bar{n}_i v)}}{15v}, \quad (8)$$

and $q_x = q_y = 1$ with $h_i(\vec{r}) = 0$. To obtain a more accurate equilibrium state the value of $q_x = q_y$ was varied for a single unit cell and n_i was relaxed via Eq. (4) until equilibrium was reached (with $h_i = 0$). In all simulations a 2D periodic box was used with grid spacing chosen to exactly fit the box, such that $\Delta x \approx 1/2$ and $\Delta y \approx 1/2$. The simulation results gave equilibrium wave numbers of $q_x = q_y = q_0^{\text{eq}} = 0.9976666$.

A. Bilayer parameter fitting

In a prior publication [17] the parameters entering Eq. (3) were chosen to best fit the DFT calculations of Zhou *et al.* [24] for various bilayer stacking configurations, as depicted in Fig. 1. For simplicity the calculations were performed assuming that the densities could be represented by only the lowest-order Fourier components needed to describe the honeycomb symmetry (i.e., Eq. (7)). However, numerical solutions of the full PFC model naturally incorporate contributions from higher-order modes. To account for this, simulations of the full model were performed in a single unit cell starting from the initial condition with $h_i = 0$ and n_i described by Eq. (7) with $(\phi, q) = (\phi_{\text{eq}}, q_0^{\text{eq}})$. The system was first relaxed in an AB type stacking (see Fig. 1), and then one layer was shifted with respect to the other and the relative heights (h_1 and h_2) were allowed to relax via Eq. (5) but not the densities n_i . Allowing the densities to vary in a non-equilibrium stacking would lead to the system relaxing back into the state of AB stacking.

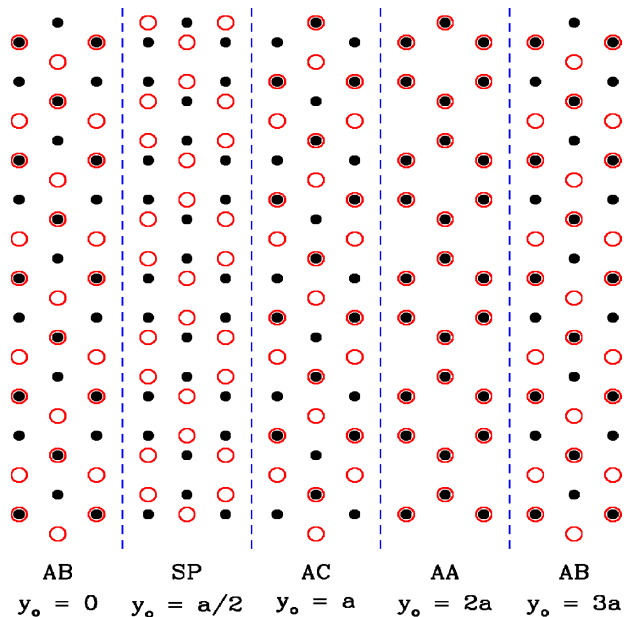


FIG. 1. Illustration of different stackings of two graphene layers with shifting distance y_0 , where the black solid (red empty) points correspond to the bottom (top) layer.

To obtain the best fit to DFT calculations the param-

Quantity	Dimensional	Dimensionless
$V_0^{(1)}$	1.43 eV/nm ²	2.72×10^{-4}
$V_0^{(2)}$	2.50 eV/nm ²	-4.72×10^{-4}
a_2	0.276 eV/nm ⁴	6.51×10^{-5}
Δ	3.47 Å	10.25
α	—	0.26

TABLE I. Summary of PFC model parameters for a Gr/Gr bilayer, as identified from the fitting to DFT calculations in Ref. [24].

eters in Eq. (3) were varied. In the work of Zhou *et al.* [24] four different types of DFT were examined. Among them three common methods were compared with the most accurate and computationally expensive (and consequently more restrictive) method named ACFDT-RPA. Their results showed that these methods generally provided qualitatively similar results (except one), which however could be considerably different quantitatively (as illustrated in Figs. 2 and 3). The reader is referred to this reference for more details. For the purpose of this work the more accurate and quantitatively reliable ACFDT-RPA results were used to parameterize the PFC model. Figures 2 and 3 compare the PFC results against all four DFT calculations of Zhou *et al.* for the stacking separation (Δh_{st}) and free energy density difference ($\Delta F_{\text{st}}/A$ per area A) with respect to the AB stacking, respectively, as a function of shifting distance y_0 . Table I summarizes the best fit PFC parameters obtained from the numerical calculations in these figures.

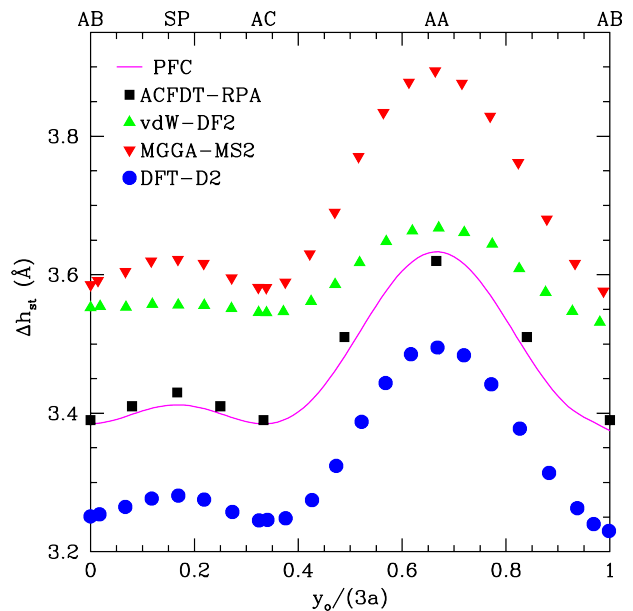


FIG. 2. Comparison of stacking height difference obtained from various DFT calculations [24] with those from the PFC bilayer model. See Fig. 1 for illustration of the stackings labelled as AB, SP, AC, and AA.

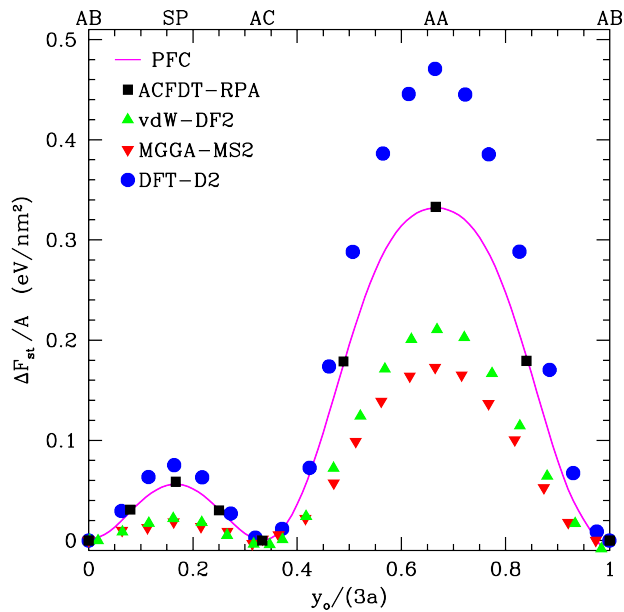


FIG. 3. Comparison of stacking free energy difference obtained from various DFT calculations [24] with those from the PFC bilayer model. For abbreviations of the different flavors of DFT, see Ref. [24]

B. Multiple-Layer Equilibrium

In this multilayer PFC model the layers are coupled only to their nearest neighbours. This implies that the free energy per unit area per layer for M layers can be written as

$$\frac{F_t}{AM} = \frac{2F_{\text{out}} + (M-2)F_{\text{in}}}{AM}, \quad (9)$$

where F_{out} and F_{in} are the free energies of the two outer and $M-2$ inner layers respectively. Thus,

$$\frac{\Delta F}{AM} = \left(1 - \frac{2}{M}\right) \frac{F_{\text{in}}}{A}, \quad (10)$$

where $\Delta F = F_t - 2F_{\text{out}}$. This was tested numerically, with results shown in Fig. 4 which verifies Eq. (10). In principle the layers could stack via an ABA or ABC sequence; however, the free energy difference between the stackings was found to be very similar, with the ABA stacking always of slightly smaller energy as shown in Fig. 4. A linear fitting to these data gives the free energy density per layer $F_{\text{in}}/A = -2.405 \times 10^{-2}$ eV/nm² for the ABA stacking and $F_{\text{in}}/A = -2.397 \times 10^{-2}$ eV/nm² for the ABC stacking.

III. DISLOCATION PAIRS IN ONE LAYER OF STACKS

In a prior study [17] the energy of a pair of dislocations in a single monolayer of graphene was examined.

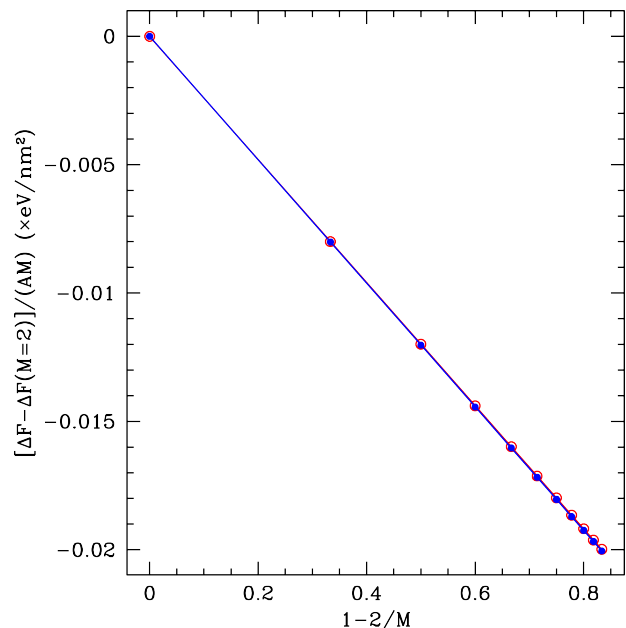


FIG. 4. Free energy density difference $\Delta F = F_t - 2F_{\text{out}}$ per layer as a function of $1 - 2/M$ with number of layers M . The solid blue (empty red) points are for ABA (ABC) stacking.

It was found that allowing for out-of-plane deformations drastically lowered the energy of the pair as compared to a vertically rigid layer. More specifically, the energy of the dislocation pair diverges with system size in the rigid case but converges in the flexible case. In what follows an examination of how dislocations in one layer influence the energetics of a multilayer system of graphene is presented. In principle the addition of layers should effectively increase the bending energy coefficient, i.e., the additional layers will suppress the bending in the defective layer, leading to a higher effective energy of the defects.

In previous work on a single defected layer, the initial condition was set with the use of Eq. (7) for n_i such that in the top (bottom) half of the 2D system q_x was chosen to fit exactly $N+1$ (N) maxima in n_i and q_y was set to q_0^{eq} everywhere. In addition, a layer of liquid ($n_i = \bar{n}_i$) of width $20\Delta x$ was inserted at the boundaries separating top and bottom halves of crystalline domains. Evolving via Eqs. (4) and (5) leads to the formation of a pair of dislocations, i.e., a dislocation dipole. However, this configuration is not feasible when coupling to other layers that are in equilibrium (such that $q_x = q_y = q_0^{\text{eq}}$). For the current simulations the simulation box was set periodic along both x and y directions and of size $L_x\Delta x \times L_y\Delta y$, where L_x and $L_y = L_x/2$ are integers. In the non-defected layers the system size was set to be $L_x\Delta x = 2Na_x$, where $a_x = 4\pi/(\sqrt{3}q_0^{\text{eq}})$ and N is an integer. In the defected layer, the q_x value of the top (bottom) half of the layer was chosen such that there were $2N+1$ ($2N-1$) maxima in the x direction. The previous single-layer defected configuration could not be used

since it would require $N+1/2$ maxima in the non-defected layers to obtain a perfect equilibrium state. The configuration used here then leads to two dislocation dipoles. Figure 5 illustrates a typical distribution of the density field n_i containing the two dipole pairs, while in Fig. 6 detailed structures of the density maxima and bonds between neighbouring maxima are shown for the four boxed regions of defects in Fig. 5.

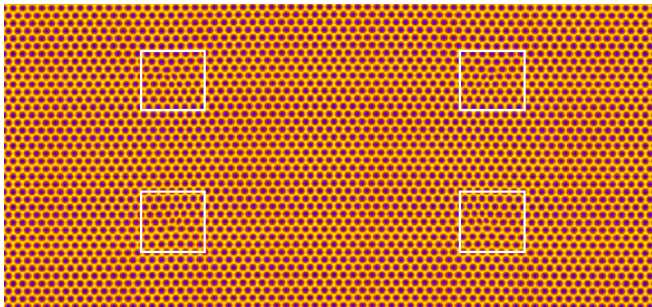


FIG. 5. Typical density-field (n_i) configuration for $N = 69$ which corresponds to a system of size $34.0 \times 17.0 \text{ nm}^2$. The boxed areas each contain one dislocation.

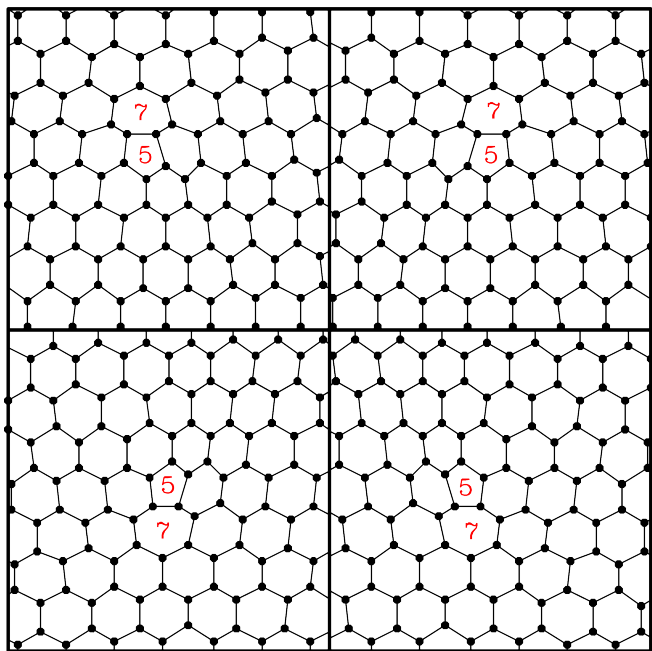


FIG. 6. Reconstruction of density maxima for the boxed regions in Fig. 5, showing the classical 5|7 dislocation structures.

One complication of such studies (single- or multi-layer) is that, in the layer that contains the defects, the initial condition gives rise to a system in which half is under tensile strain and the other half in compressive strain. More specifically this leads to a strain ε in the layer containing the defects, as given by

$$\varepsilon = \begin{cases} -1/(2N+1), & \text{if } y > L_y/2, \\ 1/(2N-1), & \text{if } y < L_y/2, \end{cases} \quad (11)$$

i.e., compressive (tensile) in the top (bottom) half of the layer. Thus to evaluate the energy of the dislocations it must be compared to the energy of strained systems. For example, if the free energy of the tensile and compressive regions is F_{ten} and F_{com} respectively, then the free energy due to the defects (F_d) is

$$F_d = F_t - (F_{\text{ten}} + F_{\text{com}})/2, \quad (12)$$

where F_t is the total free energy of the entire system given by Eq. (6).

A. Characterization of strained systems

In order to evaluate the free energy of defected systems (i.e., Eq. (12)), F_t and F^c must be calculated numerically. Since height variations in the tensile case do not lower the system free energy, in an initial setup of this system deviations of the heights from their equilibrium values can be set to zero, so that the relaxation to equilibrium is relatively rapid. In the compressive case it is useful to approximate the strain and height of the layers as a function of system size and number of layers, and then incorporate them in the initial condition.

To gain insight into the properties of the multilayer system it is useful to consider the elastic energy of the system in the small deformation limit. In a prior work [17] it was shown that in the small deformation limit the elastic contribution due to a single layer, F_{elas}^1 , can be derived from Eq. (1) by setting

$$n_i = \bar{n}_i + 2\phi_{\text{eq}} \sum_j \cos[\vec{G}_j \cdot (\vec{r} - \vec{u})], \quad (13)$$

where \vec{u} is the displacement field that enters continuum elasticity theory. In the limit of small $|\vec{\nabla}\vec{u}|$ and $|\vec{\nabla}h|$ one then gives

$$\frac{F_{\text{elas}}^1}{c_g} = \int d\vec{r} \left\{ B^x \phi_{\text{eq}}^2 \left[\frac{9}{2} (U_{xx}^2 + U_{yy}^2) + 3U_{xx}U_{yy} + 6U_{xy}^2 \right] + \frac{\kappa}{2} |\nabla^2 h|^2 \right\}, \quad (14)$$

where the strain tensor components, U_{ij} , are defined as

$$U_{\mu\nu} = \frac{1}{2} (\partial_\mu u_\nu + \partial_\nu u_\mu + h_\mu h_\nu), \quad (15)$$

where $\mu(\nu) = x$ or y . These one-mode approximation results, Eqs. (14) and (15) for single-sheet elastic free energy, are consistent with the well-known form used in the study of flexible sheets [26] and graphene monolayers [27].

For a single graphene layer with compressive strain $\varepsilon < 0$, the height of the film could be written as

$$h \approx H \cos(Qx), \quad (16)$$

with the corresponding elastic energy (F_{elas}^1 for a single layer) per unit length,

$$\frac{F_{\text{elas}}^1}{L_x c_g} = \alpha \varepsilon^2 + \frac{1}{2} \left(\frac{1}{2} \kappa Q^2 + \alpha \varepsilon \right) (QH)^2 + \frac{\alpha}{16} (QH)^4, \quad (17)$$

where $Q = 2\pi/L_x$, $\alpha = 9B^x \phi_{\text{eq}}^2/2$, and ϕ_{eq} is the equilibrium amplitude in the one-mode approximation given by Eq. (8). In this calculation the elastic free energy has been minimized with respect to the strain, resulting in a displacement field

$$u_x = \varepsilon x + H^2 Q \cos(2Qx)/8. \quad (18)$$

In a multiple-layer system within which only one layer is strained, to the lowest-order approximation

$$\Delta h_{ij} = h_i - h_j = \Delta h_{ij}^0, \quad (19)$$

which then gives for M layers,

$$\begin{aligned} \frac{F_{\text{elas}}^M}{L_x c_g} &= \frac{F_{\text{elas}}^1}{L_x c_g} + (M-1) \left[\frac{1}{4} \kappa Q^2 (QH)^2 + \frac{\alpha}{16} (QH)^4 \right] \\ &= \alpha \varepsilon^2 + \frac{1}{2} \left[\alpha \varepsilon + \frac{MQ^2}{2} \left(\kappa + \frac{\alpha}{8} H^2 \right) \right] (QH)^2 \end{aligned} \quad (20)$$

for the compressive case. The free energy of the tensile case is just Eq. (20) with $H = 0$, i.e.,

$$F_{\text{elas}}^M / (L_x c_g) = \alpha \varepsilon^2, \quad (21)$$

where it has been explicitly assumed that all layers buckle with the same amount, which would be valid in the limit of large a_2 . Minimizing with respect to H then gives

$$H^2 = -2 \left(\frac{2\varepsilon}{MQ^2} + \frac{\kappa}{\alpha} \right). \quad (22)$$

This equation only has a solution if (for compressive strain with $\varepsilon < 0$)

$$\frac{|\varepsilon|}{Q^2} > \frac{M\kappa}{2\alpha}, \quad (23)$$

naturally showing that if the number of layers increases it becomes more difficult to bend the multilayer structure.

Substituting Eq. (22) into Eq. (20) gives

$$\frac{F_{\text{elas}}^M}{L_x c_g} = \frac{M-1}{M} \alpha \varepsilon^2 - \kappa Q^2 \left(\varepsilon + M \frac{\kappa Q^2}{4\alpha} \right), \quad (24)$$

which is valid only if Eq. (23) is satisfied; otherwise the solution reduces to Eq. (21).

A comparison of this prediction with direct numerical simulations of the full model is shown in Fig. 7 for H (for the compressive case), and in Figs. 8 and 9 for F_{elas}^M/L_x (for the tensile and compressive cases respectively). These figures indicate that the above approximate analytic results generally agree with simulation results. The one anomaly is for H at a system size of

$N = 17$ which corresponds to a relatively large strain of 5.56% and 6.25% in the compressive and tensile regions respectively. It should also be noted that the full-order profiles of height h , obtained from the numerical data, indicate the contributions from higher-order modes beyond the approximation of Eq. (16). Nevertheless the close agreement between the analytic and numerical results validate the calculations.

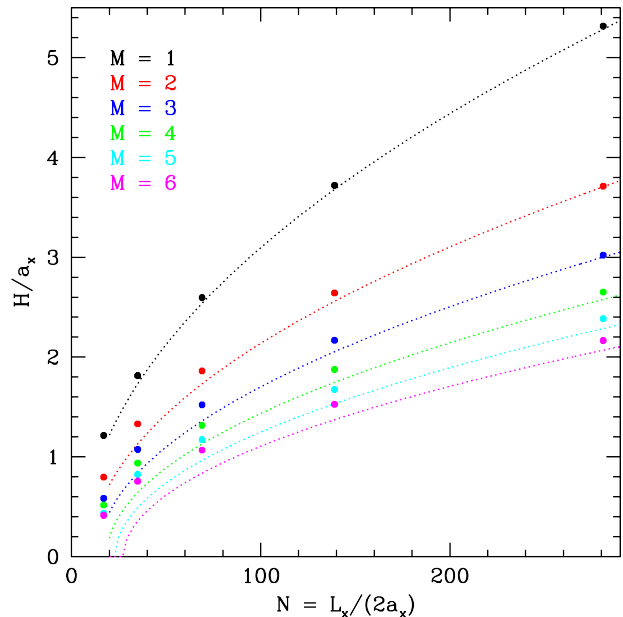


FIG. 7. Height variation amplitude as a function of system size for different number of layers in the compressive case. Symbols represent the results obtained from numerical simulations of the full model, and lines are evaluated from Eq. (22).

B. Dislocation dipole pair energy

In this section the influence of the number of layers (M) and system size (N) in a multilayer stacked system which contains one defected layer is examined. The defected layer was placed as close as possible to the middle of the stack, i.e., directly in the middle for an odd number of layers or one more layer on one side for an even number of layers. The other layers were initialized as perfect crystalline states in an AB stacking when possible. While it would be never possible to know if the state that emerges from a numerical simulation is the lowest possible energy state, several approaches were taken to identify this state.

The first approach was to relax one single layer containing the defects and then add another layer, and relax the system; then add one more layer and relax again until a total of five layers had been added to the original defected layer. As stated earlier the defected layer was always placed in the middle of the stack (or closest in the case of an even number of layers). The second method

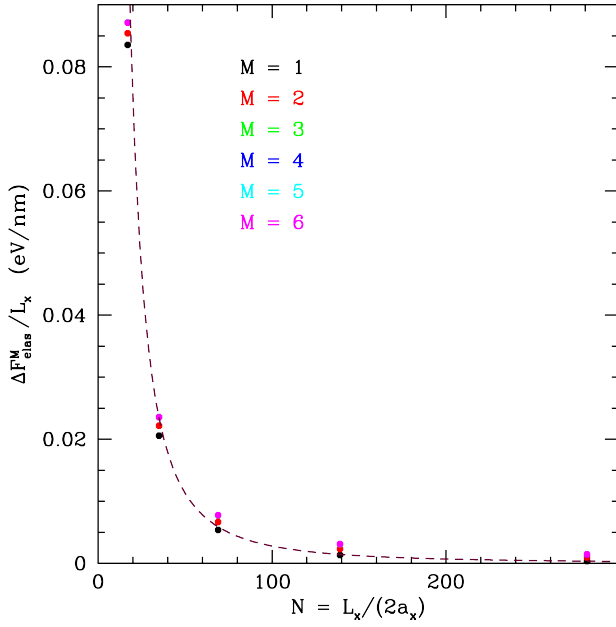


FIG. 8. Elastic free energy per length as a function of system size for different number of layers in the tensile case. Symbols represent the results obtained from numerical simulations of the full model, and lines are evaluated from Eq. (21).

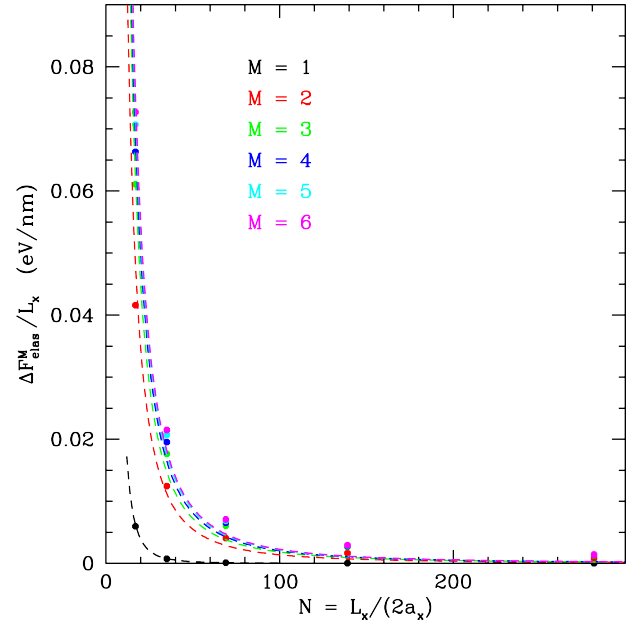


FIG. 9. Elastic free energy per length as a function of system size for different number of layers in the compressive case. Symbols represent the results obtained from numerical simulations of the full model, and lines are evaluated from Eq. (24).

was to relax each stack independently (e.g., not rely on using a $M = 2$ stack as an initial condition for a $M = 3$ stack). These approaches led to two distinct configurations which will be termed Type I and Type II. Figure 10 illustrates a Type I configuration in which the height increases at both defect pairs. In contrast, in a Type II configuration (Fig. 11) the height is positive on one side (in the x direction) of the defect pair and negative on the other side.

Which configuration gives the lowest energy is determined by the competition between local dislocation core energy and elastic strain energy in the surrounding layers. Typically the Type II configuration leads to a lower core energy and a larger strain energy. For the example given in Figs. 10 and 11 with $(M, N) = (2, 139)$, the average core energy density (defined as the average energy density in a radius of 3.4 \AA around the core) was -1.1533 eV/\AA^2 for the Type I configuration and -1.1544 for the Type II case. The average volumetric stress (defined as $\sigma_V = \sigma_{xx} + \sigma_{yy}$) was 0.0891 eV/\AA^2 for Type I and 0.1056 eV/\AA^2 for Type II. In this example the Type II configuration had the lowest total free energy.

Figures 12–15 depict the configurations that minimized the system free energy for system sizes ranging from $N = 35$ to $N = 281$. To further check that the lowest energy states were found, initial condition incorporating final Type I or II configurations were considered. For example, a layer could be added to Fig. 14(b) producing Type II initial condition for three-layer systems, or a layer could be stripped from Fig. 14(c), producing a Type I initial condition for a two-layer system. Although

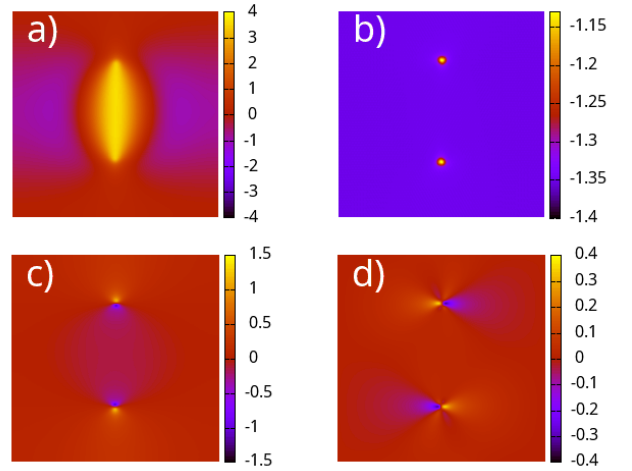


FIG. 10. Illustration of Type I structure in a bilayer system with $N = 139$ ($L_x = 69 \text{ nm}$), for the spatial profiles of (a) height (color-bar scale in \AA), (b) free energy density, (c) volumetric stress $\sigma_{xx} + \sigma_{yy}$, and (d) shear stress σ_{xy} . In (b)–(d) the color-bar scale is eV/\AA^2 . Note that only half of the simulation box is depicted here, and (a), (c), and (d) are for the defected layer while (b) is for the free energy density of the total system.

it was computationally expensive to check the energy of every system simulated, care has been taken to sample a number of different states. At the end it became clear that the Type I configuration was the lowest energy state when the multi-layer stack consists of more than three layers. This is due to the fact that more elastic energy is

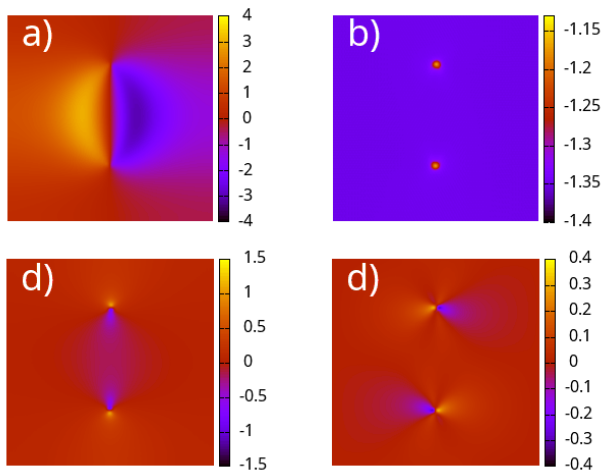


FIG. 11. Illustration of Type II structure in a bilayer system with $N = 139$ ($L_x = 69$) nm. The quantities shown in panels (a)-(d) are the same as those in Fig. 10, with the same color-bar scales.

added with each additional layer, since the defected layer causes out-of-plane fluctuations in other layers. Thus as the number of layers increases the elastic strain energy dominates over the dislocation core energy (which exists only in the one defected layer), for which the Type I configuration exhibits lower strain energy density. In addition, for $M > 3$, initial conditions containing Type II defects would eventually decay into Type I defects. However, for small M the energy difference between Type I and Type II defects was very small, indicating that thermal fluctuations may play an important role for $M \leq 3$.

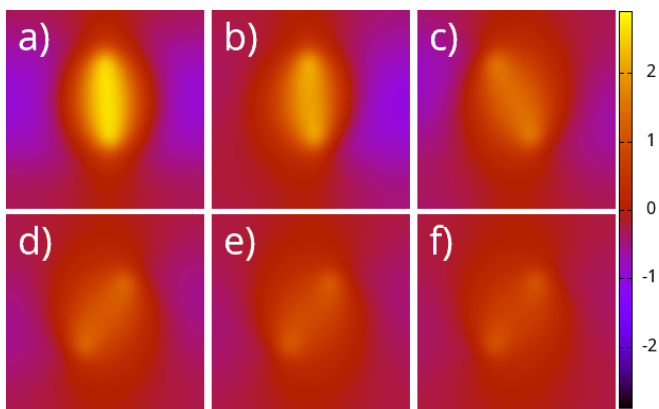


FIG. 12. Height profile of the layer containing dislocations with $N = 35$ ($L_x = 17$ nm), corresponding to various multi-layer systems with $M = 1$ to 6 layers in (a)-(f) respectively. Only half of the system is shown in each panel. The color-bar scale is in \AA and the average height of the layer has been subtracted.

The defect free energy F_d , defined by Eq. (12), for all systems studied is summarized in Fig. 16. As can be seen in this figure, for large enough system sizes the de-

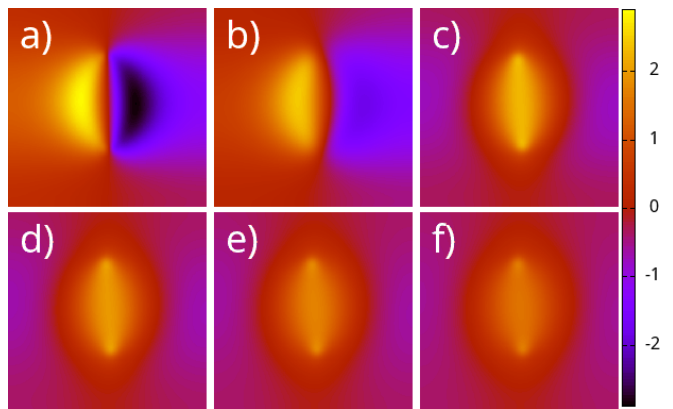


FIG. 13. Height profile of the layer containing dislocations with $N = 69$ ($L_x = 34$ nm) and the setup similar to Fig. 12, for $M = 1$ to 6 layers in (a)-(f) respectively.

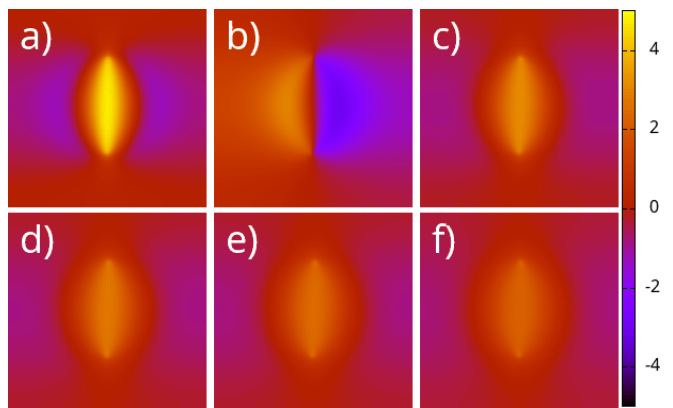


FIG. 14. Height profile of the layer containing dislocations with $N = 139$ ($L_x = 69$ nm) and the setup similar to Fig. 12, for $M = 1$ to 6 layers in (a)-(f) respectively.

fect free energy increases rapidly as the number of layers is added up to three layers and then rises at a slower rate before starting to saturate. The one exception was at the smallest system examined ($N = 35$ with $L_x = 17$ nm). Inspection of the corresponding configurations (Fig. 12) reveals strong finite size effects. It is clear that in this case the dipoles (particularly for $M \geq 3$) tilt away from the vertical y orientation to lower the energy. This also occurred in the next biggest system size ($N = 69$ with $L_x = 34$ nm) but to a much less extent, while this tilting phenomenon is not apparent in the two other largest systems examined.

For the three largest systems simulated F_d was fit to the form $F_d = F_d^\infty [1 - \exp(-aM - b)]$, where F_d^∞ , a , and b are fitting parameters that can be used to estimate the value of $\Delta F_\infty = \Delta F(M \rightarrow \infty)$ which is the energy difference between ideal bulk and that with one defected layer. These fits (shown in Fig. 16) give $\Delta F_\infty = 37.71$ eV, 40.04 eV, and 41.44 eV for $L_x = 17$ nm, 34 nm, and 138 nm respectively. This implies that the maximum increases of defect energy (i.e., at the $M = \infty$ limit)

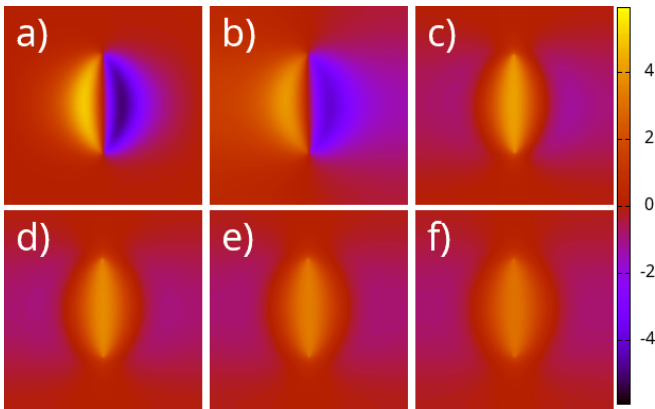


FIG. 15. Height profile of the layer containing dislocations with $N = 281$ ($L_x = 138$ nm) and the setup similar to Fig. 12, for $M = 1$ to 6 layers in (a)–(f) respectively.

are given by $F_d^\infty/F_d(M=1) = 1.24, 1.29,$ and 1.34 for $L_x = 17$ nm, 34 nm, and 138 nm respectively. This fit also gives an estimate of how many layers it takes to almost reach the saturate value of infinite M . From the fitting results, it was found that the number of layers needed for ΔF_d to reach 99% of ΔF_∞ was approximately $M = 6, 10,$ and 9 for $L_x = 34$ nm, 69 nm, and 138 nm respectively.

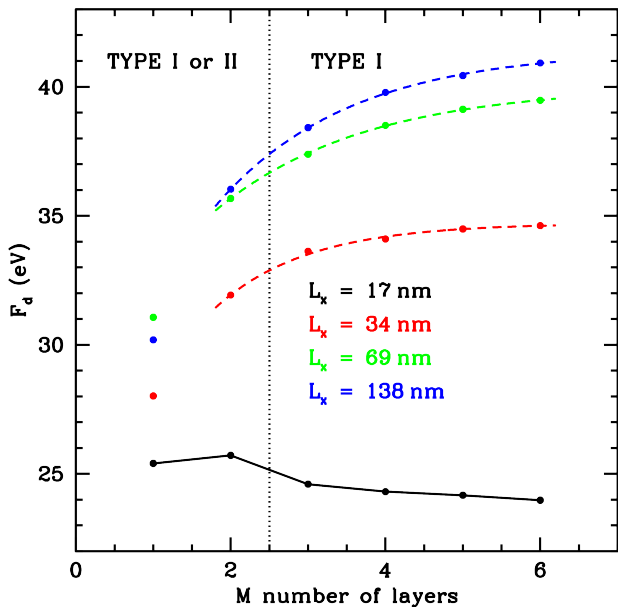


FIG. 16. The free energy difference of multilayer system (with two dislocation pairs) as a function of the number of layers (M) for various system sizes. The red, green, and blue dashed lines are fits to the functional form $F_d = F_d^\infty [1 - \exp(-aM - b)]$, where F_d^∞ , a , and b are fitting parameters.

To further explore the influence of the defected layer on the other layers, the volumetric stress, $\sigma_V = \sigma_{xx} + \sigma_{yy}$, is shown in Fig. 17 for each layer of a $M = 6$ stack

with $N = 281$. This figure shows how stress in the defected layer is mirrored in the surrounding layers, although with smaller magnitudes (by roughly a factor of fifteen). The height difference ($\Delta h_{ij} = h_i - h_j$) near one of the dislocation cores is illustrated for this same system in Fig. 18, which is constructed such that the color-bar scale is $\Delta h_{AB} \pm \Delta$ with Δ depending on the layer differences and $\Delta h_{AB} = 3.3845$ Å the equilibrium height difference for a AB stacking. With this scale the height difference of Δh_{AB} appears red in the figures. This figure indicates that Δh_{ij} is larger below the defected layer and smaller above. This can be understood by considering that the height of the defected layer is higher near the dislocation core, causing the height of all the layers to increase near the core. However, since this induces strain, the layer heights do not increase enough to reach Δh_{AB} , which leads to height differences above (below) the defected layer to be smaller (larger) than the value of Δh_{AB} .

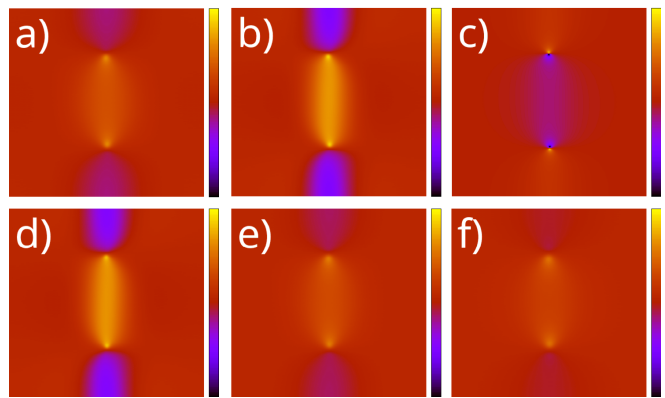


FIG. 17. Volumetric stress for a six-layer stack with $N = 281$ ($L_x = 138$ nm). (a)–(f) correspond to layer one to six respectively (where layer three in (c) is the defected layer). The color-bar scales in (a), (b), (d)–(f) are from -0.1 eV/nm² to 0.1 eV/nm², and in (c) from -1.5 eV/nm² to 1.5 eV/nm². Note that only half of the simulated system is shown here.

IV. DISCUSSION AND SUMMARY

In this work the influence of four 5|7 dislocations (i.e., two dislocation dipole pairs) in one layer within an otherwise perfect stack of graphene layers has been examined. The parameters entering the PFC model were matched to the stacking heights and energies calculated by DFT (given in Ref. [24]) to provide quantitative predictions for the system. Care was taken to find the equilibrium states with one layer strained (compressive or tensile) in the stack to provide a reference state to compare with stacks containing one layer with the 5|7 dislocations.

When the initial condition was such that four dislocation defects emerged, it was found that the defected layer had a strong impact on the other surrounding layers as

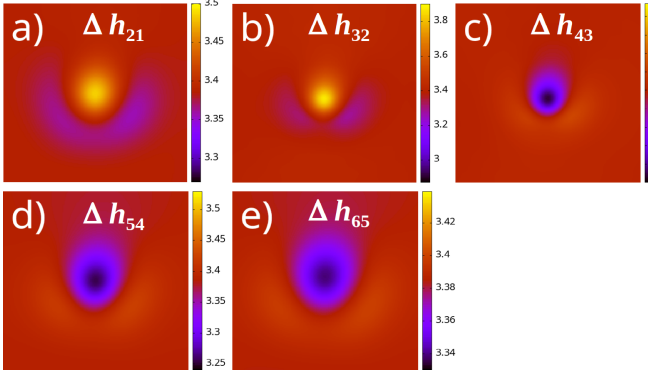


FIG. 18. Height difference ($\Delta h_{ij} = h_i - h_j$) between layers around one dislocation core (of size $6.8 \text{ nm} \times 6.68 \text{ nm}$) for a stack of six layers with $N = 281$ ($L_x = 138 \text{ nm}$).

the out-of-plane deformation created by the dislocations in the “middle” layer led to deformations in the surrounding layers, which effectively increases the elastic energy of the system. Two different solutions (Type I and Type II) of multilayer configurations have been identified, one with a lower dislocation core energy (Type II) and the other with a lower far field elastic energy (Type I). As the number of layers in the stack was increased the Type I configuration was always of lowest energy for all the system sizes considered, which is consistent with the fact that far field elastic energy in the stack increases with the number of layers added.

Quantitative predictions have been made for the free energy difference, F_d , of a stack of Gr layers containing one defected layer compared to the defect-free system. In general it was found that F_d increased with system size as was seen in the case of single sheets [17]. In addition, F_d increased with the number of layers (M) and appears to saturate at some finite value of $M^s \approx 10$. To some extent M^s can be considered as the distance over which the defected layer influences the entire system. In addition, for the system sizes studied here our calculations showed that inclusion of the four dislocation defects in one embedded layer increased defect energy by a maximum of 34% in the largest film studied.

ACKNOWLEDGMENTS

K.R.E. acknowledges support from the National Science Foundation (NSF) under Grant No. DMR-2006456, Oakland University Technology Services and high-performance research computing facility (Matilda), and Aalto Science Institute for support during his visit. Z.-F.H. acknowledges support from NSF under Grant No. DMR-2006446. T.A-N. has been supported in part by the Academy of Finland through its Quantum Technology Finland CoE Grant No. 312298 and the European Union

– NextGenerationEU instrument Grant No. 353298. The authors wish to acknowledge CSC – IT Center for Science, Finland, for generous computational resources and the CSC HPC support group for helping setup and run the PFC solver. The authors would like to thank Cristian Achim for useful discussions and CUDA code development. We would also like to thank Arsalan Hashemi for useful discussions and carrying out additional DFT calculations for stacked graphene layers.

Appendix A: Functional Derivatives

Defining F^c as the free energy due to the coupling between layers, i.e.,

$$F^c = \sum_{i=1}^{M-1} \mathcal{F}_{i+1,i}^c, \quad (\text{A1})$$

gives

$$\begin{aligned} \frac{\delta F_c}{\delta n_i} &= V_0(\delta n_{i-1} + \delta n_{i+1}) \\ &\quad - 2a_2 \Delta \alpha [(\Delta h_{i,i-1} - \Delta h_{i,i-1}^0) \delta n_{i-1} \\ &\quad + (\Delta h_{i+1,i} - \Delta h_{i+1,i}^0) \delta n_{i+1}], \end{aligned} \quad (\text{A2})$$

for $i \neq 1$ or $i \neq N$, while for $i = 1$,

$$\frac{\delta F_c}{\delta n_1} = V_0 \delta n_2 - 2a_2 \Delta \alpha (\Delta h_{2,1} - \Delta h_{2,1}^0) \delta n_2, \quad (\text{A3})$$

and for $i = N$

$$\begin{aligned} \frac{\delta F_c}{\delta n_N} &= V_0 \delta n_{N-1} \\ &\quad - 2a_2 \Delta \alpha (\Delta h_{N,N-1} - \Delta h_{N,N-1}^0) \delta n_{N-1} \end{aligned} \quad (\text{A4})$$

The functional derivatives with respect to height h_i are given by: for $i = 1$,

$$\begin{aligned} \frac{\delta F_c}{\delta h_1} &= -2a_2 [h_2 - h_1 - \Delta h_{1,2}^0] \\ &= 2a_2 [h_1 - h_2 + \Delta h_{1,2}^0], \end{aligned} \quad (\text{A5})$$

for $i = N$,

$$\frac{\delta F_c}{\delta h_N} = 2a_2 [h_N - h_{N-1} - \Delta h_{N,N-1}^0], \quad (\text{A6})$$

and for $i \neq 1$ or $i \neq N$,

$$\begin{aligned} \frac{\delta F_c}{\delta h_i} &= 2a_2 [h_i - h_{i-1} - \Delta h_{i,i-1}^0 - h_{i+1} + h_i + \Delta h_{i,i+1}^0] \\ &= 2a_2 [2h_i - h_{i-1} - h_{i+1} + \Delta h_{i,i+1}^0 - \Delta h_{i,i-1}^0] \end{aligned} \quad (\text{A7})$$

-
- [1] K. S. Nonoselov, S. V. Morozov, D. Jiang, Y. Zhang, S. V. Dubonos, I. V. Grigorieva, and A. A. Firsov, Electric field effect in atomically thin carbon films, *Science* **22**, 5696 (2004).
- [2] G. S. Jing-Yang You, Bo Gu and Y. P. Feng, Two-dimensional topological superconductivity candidate in a van der waals layered material, *Phys. Rev. B* **103**, 104503 (2021).
- [3] D. M. K. S. Burch and J.-G. Park, Magnetism in two-dimensional van der waals materials, *Nature* **599**, 582 (2021).
- [4] P. Hirvonen, H. Vili, H. Dong, Z. Fan, K. R. Elder, and T. Ala-Nissila, Phase-field crystal model for heterostructures, *Phys. Rev. B* **100**, 165412 (2019).
- [5] Z. Zhang, P. Chen, X. Duan, K. Zang, J. Luo, and X. Duan, Robust epitaxial growth of two-dimensional heterostructures, multiheterostructures, and superlattices, *Science* **357**, 788 (2017).
- [6] Z.-F. Huang, Atomic ordering and phase separation in lateral heterostructures and multijunctions of ternary two-dimensional hexagonal materials, *Phys. Rev. Materials* **6**, 074001 (2022).
- [7] W. Ouyang, O. Hod, and M. Urbakh, Parity-dependent moiré superlattices in graphene/h-BN heterostructures: A route to mechanomutable metamaterials, *Phys. Rev. Lett.* **126**, 216101 (2021).
- [8] V. Vaño, M. Amini, S. C. Ganguli, G. Chen, J. L. Lado, S. Kezilebieke, and P. Liljeroth, Artificial heavy fermions in a van der waals heterostructure, *Nature* **573**, 57 (2021).
- [9] R. W. Havener, Y. Liang, L. Brown, L. Yang, and J. Park, Van hove singularities and excitonic effects in the optical conductivity of twisted bilayer graphene, *Nano Lett.* **14**, 3353 (2014).
- [10] F. Guinea and N. R. Walet, Electrostatic effects, band distortions, and superconductivity in twisted graphene bilayers, *PNAS* **115**, 13174 (2018).
- [11] E. Y. Andrei and A. H. MacDonald, Graphene bilayers with a twist, *Nat. Mater.* **19**, 1265 (2020).
- [12] K. Azizi, P. Hirvonen, Z. Fan, A. Harju, K. R. Elder, T. Ala-Nissila, and S. M. V. Allaei, Kapitza thermal resistance across individual grain boundaries in graphene, *Carbon* **125**, 384 (2017).
- [13] H. Dong, P. Hirvonen, Z. Fan, and T. Ala-Nissila, Heat transport in pristine and polycrystalline single-layer hexagonal boron nitride, *Phys. Chem. Chem. Phys.* **20** (2018).
- [14] C. Gong, S. Lee, S. Hong, E. Yoon, G.-D. Lee, and J. H. Warner, Point defects in turbostratic stacked bilayer graphene, *Nanoscale* **9**, 13725 (2017).
- [15] S. Choi, B. W. Jeong, S. Kim, and G. Kim, Monovacancy-induced magnetism in graphene bilayer, *J. Phys: Condens. Matter* **20**, 235220 (2008).
- [16] A. Mohapatra, S. Das, K. Mujumdar, M. S. R. Rao, and M. Jaiswal, Thermal transport across wrinkle in few-layer graphene stacks, *Nanoscale Adv.* **3**, 1708 (2021).
- [17] K. R. Elder, C. V. Achim, V. Heinonen, E. Granato, S. C. Ying, and T. Ala-Nissila, Modeling buckling and topological defects in stacked two-dimensional layers of graphene and hexagonal boron nitride, *Phys. Rev. Mat.* **5**, 034004 (2021).
- [18] S. Chen and D. C. Chrzan, Continuum theory of dislocations and buckling in graphene, *Phys. Rev. B* **84**, 214103 (2011).
- [19] O. V. Yazyev and S. G. Louie, Topological defects in graphene: Dislocations and grain boundaries, *Phys. Rev. B* **81**, 195420 (2010).
- [20] Y. Liu and B. I. Yakobson, Cones, pringles, and grain boundary landscapes in graphene topology, *Nano Lett.* **10**, 2178 (2010).
- [21] E. Granato, K. R. Elder, S. C. Ying, and T. Ala-Nissila, Dynamics of fluctuations and thermal buckling in graphene from a phase-field crystal model, *Phys. Rev. B* **107**, 035428 (2023).
- [22] E. Granato, M. Greb, K. R. Elder, S. C. Ying, and T. Ala-Nissila, Dynamics scaling of out-of-plane fluctuations in free standing graphene, *Phys. Rev. B* **105**, L201409 (2022).
- [23] K. R. Elder, Z.-F. Huang, and T. Ala-Nissila, Moire patterns and inversion boundaries in graphene/hexagonal boron nitride bilayers, *Phys. Rev. Mat.* **7**, 024003 (2023).
- [24] S. Zhou, J. Han, S. Dai, J. Sun, and D. J. Srolovitz, van der waals bilayer energetics: Generalized stacking-fault energy of graphene, boron nitride, and graphene/boron nitride bilayers, *Phys. Rev. B* **92**, 155438 (2015).
- [25] N. Provatas and K. Elder, *Phase-Field Methods in Materials Science and Engineering* (Wiley-VCH Verlag GmbH, 2010).
- [26] D. R. Nelson and L. Peliti, Fluctuations in membranes with crystalline and hexatic order, *Journal de Physique* **48**, 1085 (1987).
- [27] J. H. Los, M. I. Katsnelson, O. V. Yazyev, K. V. Zakharchenko, and A. Fasolino, Scaling properties of flexible membranes from atomistic simulations: Application to graphene, *Phys. Rev. B* **80**, 121405(R) (2009).